Predicting plasmonic enhancement of photoluminescence with a multi-scale and multi-physics numerical method

Raonaqul Islam[1], Qing H. Liu[2], and Ergun Simsek[1]

[1]University of Maryland Baltimore County, 1000 Hilltop Circle, 21250 Baltimore, MD, USA
[2]Eastern Institute of Technology, Ningbo, Zhejiang Province, China

ABSTRACT

Monolayer transition-metal dichalcogenides (TMDs) are promising ultrathin light emitters, but their intrinsically weak light–matter interaction limits achievable radiative efficiency, motivating the use of plasmonic nanostructures to enhance photoluminescence (PL) and electroluminescence (EL). While extensive experimental work has established that such enhancement arises from a combination of near-field excitation enhancement, Purcell-accelerated radiative decay, and charge-transfer-driven exciton/trion redistribution, no existing numerical framework self-consistently couples all three underlying physical timescales to directly predict the resulting emission spectra. Here, we develop a multiscale simulation framework that couples a finite-difference time-domain (FDTD) electromagnetic solver, a semiconductor drift-diffusion transport model, and bright/dark exciton rate equations through an operator-splitting outer loop. Cycle-averaged optical generation rates and Purcell-renormalized radiative lifetimes extracted from the electromagnetic layer drive the exciton population dynamics, which in turn source an incoherent dipole emission current that re-enters the electromagnetic solver. For bare monolayer MoS_2 and WSe_2, we find that the ∼9-fold difference in peak PL intensity substantially overstates the true emission contrast: once linewidth and population dynamics are accounted for via the total time-integrated PL, WSe_2 emits only ∼5.3 times more strongly than MoS_2 under identical illumination. Applied to MoS_2 coupled to a periodic Au grating, the framework predicts a ∼35-fold PL enhancement, arising from competing effects: a two-orders-of-magnitude gain in bright-exciton population offset by a five-fold reduction in internal quantum yield due to metal-induced non-radiative quenching. This enhancement is accompanied by a Purcell-accelerated population buildup time, which is qualitatively consistent with experimentally measured lifetime reductions in analogous plasmonic geometries. The framework further reproduces the strong polarization dependence intrinsic to plasmonic gratings, showing enhancement only for the polarization supporting localized surface plasmon resonances. These results establish a predictive, self-consistent multiphysics tool for the rational design of plasmonically enhanced light emitters from two-dimensional materials.

Keywords: photoluminescence, 2D materials, plasmonic enhancement, numerical model, FDTD.

1. INTRODUCTION

Monolayer transition-metal dichalcogenides (TMDs) such as molybdenum disulfide (MoS_2) and tungsten diselenide (WSe_2) are direct-bandgap semiconductors whose photoluminescence (PL) and electroluminescence (EL) make them attractive for ultrathin light-emitting and sensing applications.[1,2] However, their intrinsically weak light–matter interaction, a consequence of atomic-scale thickness, limits the radiative efficiency achievable in practical devices. Plasmonic nanostructures have emerged as one of the most effective routes to overcome this limitation,[3–8] since the strong near-field confinement and Purcell-enhanced radiative decay rates they provide can be tailored to spectrally and spatially overlap with the excitonic transitions of the underlying 2D material. Figure 1(a) and (b) illustrate a representative plasmonically enhanced PL configuration and the corresponding FDTD simulation domain used in this work.

Experimental demonstrations of plasmon-enhanced TMD emission span a wide range of architectures and enhancement mechanisms. Irfan *et al.* compared few-layer MoS_2 decorated with anisotropic Au nanorods (NRs)

Further author information: (Send correspondence to E. S.)
E-mail: simsek@umbc.edu, Telephone: +1 (410) 455 3540

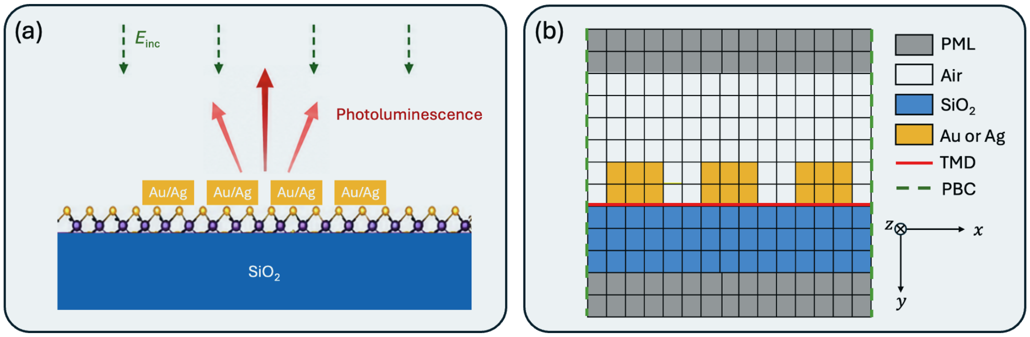

Figure 1: Schematic of the plasmonically enhanced PL configuration and corresponding FDTD simulation domain. (a) A monolayer TMD (MoS_2 or WSe_2) on a SiO_2 substrate is excited by a normally incident field $\mathbf{E}_{\text{inc}}$, with metal (Au or Ag) nano-rods placed above the TMD to plasmonically enhance the emitted luminescence. (b) Two-dimensional Yee grid representation of the FDTD simulation domain corresponding to (a), showing the discretized layers of air, SiO_2 substrate, TMD monolayer (red line), and periodically arranged Au/Ag nanostructures. Periodic boundary conditions (PBC, green dashed lines) are applied on the left and right boundaries to model an infinite array of nanostructures using a single unit, while perfectly matched layers (PML, gray) truncate the top and bottom boundaries to absorb outgoing radiation.

versus isotropic Au nanospheres (NSs) of comparable diameter and found that NRs produced roughly twice the PL enhancement of NSs (4.3-fold versus 2-fold), a difference attributed to the highly localized hot spots at the NR tips associated with the longitudinal surface plasmon resonance; deconvolution of the PL spectra further revealed a trion feature unique to the NR-decorated samples, indicating that hot-electron injection and consequent n-type doping contribute alongside near-field amplification.[7] Lee *et al.* systematically varied the areal density of Au NRs spectrally tuned to the MoS_2 direct-gap emission and observed a non-monotonic PL response, with enhancement peaking near a factor of 6.5 at intermediate density before declining at higher coverage due to competition between plasmonic near-field coupling and metal-induced shielding/absorption.[3] Layer-thickness-dependent studies of Au-aggregate/MoS_2 hybrids by Yan *et al.* showed that the sign of the net PL response can invert between quenching (thin flakes, dominated by photoexcited-electron injection into the metal) and up to 5.5-fold enhancement (thick flakes, dominated by near-field Purcell enhancement), with the two channels approximately canceling at intermediate thickness.[4,5] More recently, Gautam *et al.* demonstrated wafer-scale, resist-free plasmonic gratings achieving PL enhancement exceeding 390-fold through efficient exciton–plasmon coupling, with time-resolved measurements showing a room-temperature lifetime reduction from 0.595 ns to 0.130 ns that directly confirms Purcell-accelerated radiative recombination as the dominant mechanism,[8] while single-particle gold nanorod–WS_2 heterostructures studied by Jiang *et al.* have revealed clear mode-splitting and up to three-orders-of-magnitude PL enhancement in the intermediate plasmon–exciton coupling regime.[9] Nanowire-dimer gap antennas have additionally demonstrated that substantial Purcell enhancement can be realized even for emitters positioned away from the plasmonic hot spot, avoiding the fluorescence quenching that typically accompanies direct metal contact.[10] Collectively, these studies indicate that plasmonically enhanced PL in TMDs arises from at least three partially separable channels: near-field enhancement of absorption, Purcell-effect acceleration of radiative recombination, and hot-electron/charge-transfer-driven redistribution of bright-exciton, dark-exciton, and trion populations, whose relative weight depends sensitively on spectral overlap, emitter–metal geometry, and TMD thickness/doping state. This motivates a predictive numerical framework capable of self-consistently capturing all three effects across their disparate characteristic time scales.

Despite this motivation, quantitative computational modeling of TMD luminescence remains challenging because the relevant physics spans at least four decades in time, from femtosecond optical cycles through picosecond carrier thermalization and exciton formation to nanosecond radiative lifetimes, and existing numerical work aimed at directly predicting PL spectra (rather than only radiative lifetimes or enhancement factors) falls largely into two categories: first-principles calculations of intrinsic radiative properties, and semiclassical/device-level models of exciton and free-carrier dynamics. Classical electromagnetic solvers, such as the ones based on the finite-difference time-domain (FDTD) method,[11–14] naturally operate at the optical-cycle timescale and encode material dispersion correctly via the Lorentz-Drude model and the auxiliary differential equation (ADE) formalism, but they are strictly linear and contain no notion of incoherent carrier populations or spontaneous emission. Semiconductor drift-diffusion solvers[12–14] resolve carrier transport on picosecond timescales but treat photons only through generation and loss rates, missing both the vectorial structure of the optical field and photonic environment effects such as Purcell enhancement; the underlying carrier continuity equations are typically discretized using the exponentially fitted Scharfetter–Gummel scheme, which remains the standard numerically stable approach for coupling drift-diffusion transport to a self-consistent electrostatic solution in the presence of steep carrier-density gradients, such as those expected at a plasmonically enhanced generation hot spot.[15] We previously developed a compact numerical method for simulating MoS_2 phototransistors that self-consistently couples optical absorption to carrier transport,[12] and subsequently extended this approach to plasmonically enhanced 2D-material phototransistors under strong optical excitation by explicitly coupling an electromagnetic near-field solver to a drift-diffusion transport model.[13] Although these studies target photodetection rather than emission, they establish the same core multiphysics coupling strategy: an electromagnetic-field solution feeding into a carrier transport/generation model for a 2D material under a metallic nanostructure. The present framework extends this strategy to the emission problem. At the opposite end of the modeling hierarchy, first-principles approaches based on density functional theory, often combined with the many-body GW-Bethe–Salpeter-equation (BSE) formalism, provide the most rigorous treatment of exciton binding energies, oscillator strengths, and intrinsic radiative lifetimes in monolayer TMDs, as demonstrated by Palummo *et al.*, who obtained zero-temperature radiative lifetimes on the order of tens of femtoseconds for the lowest-energy bright exciton and showed how thermal averaging over the exciton dispersion within the light cone extends these to the picosecond and sub-nanosecond scales observed at room temperature.[16] Bridging these two regimes, Wang *et al.* developed an analytical/numerical model for the radiative decay rates of excitons and trions in monolayer MoS_2 by treating them as oscillating in-plane dipoles radiating into the surrounding dielectric environment, yielding closed-form expressions for the radiative lifetime as a function of dielectric environment, exciton momentum, and temperature;[17] because this class of model expresses the radiative rate in terms of quantities (oscillator strength, local dielectric environment, momentum-space light cone) that can be evaluated within a coupled electromagnetic-transport framework rather than requiring a full many-body calculation at every spatial grid point, it forms a natural bridge between microscopic BSE-level exciton physics and the macroscopic, spatially resolved excitonic density equations used here. While such first-principles and semiclassical results are indispensable for benchmarking the excitonic parameters (binding energy, transition dipole moment, zero-temperature radiative rate) that enter the excitonic rate-equation layer of a multiscale framework, their computational cost or reduced dimensionality precludes direct application to the micron-scale, spatially inhomogeneous plasmonic geometries and device-level carrier transport considered here; consequently, they are best used as inputs or calibration points for the semiclassical excitonic and transport models rather than as a replacement for them. To our knowledge, no prior numerical framework has self-consistently coupled all three time scales (electromagnetic near-field/Purcell enhancement, drift-diffusion carrier transport, and bright/dark exciton population dynamics) to directly predict plasmonically enhanced PL spectra of monolayer TMDs, which is the gap the present work addresses.

In this work, we develop and apply such a multiscale FDTD/drift-diffusion/excitonic-density simulation framework to model plasmonically enhanced PL from monolayer TMDs coupled to metallic nanostructures. Rather than treating the electromagnetic, transport, and excitonic layers as independent calculations stitched together *a posteriori*, our framework couples them through an operator-splitting outer loop in which cycle-averaged optical generation rates and Purcell-renormalized radiative lifetimes, extracted directly from the FDTD solution, are fed into the drift-diffusion and bright/dark exciton rate equations at each time step, while the resulting exciton population in turn sources an incoherent dipole current that re-enters the electromagnetic solver. This bidirectional coupling allows the model to capture, self-consistently and within a single simulation, the near-field enhancement of absorption, the Purcell-driven acceleration of spontaneous emission, and the doping- and defect-mediated redistribution between bright excitons, dark excitons, and trions that together determine the net PL response observed experimentally.

The remainder of this manuscript is organized as follows: Section 2 describes the implementation of our multiscale numerical model, including the electromagnetic, drift-diffusion, and excitonic rate-equation layers and their coupling; Section 3 presents numerical results; and in Section 4, we conclude.

2. IMPLEMENTATION

The implementation couples three physical layers, each operating on its own characteristic timescale, into a single multiscale multiphysics framework that predicts plasmonically enhanced photoluminescence from a monolayer transition-metal dichalcogenide (TMD, MoS_2 or WSe_2) placed beneath a periodic array of Au nanorods acting as a plasmonic grating as illustrated in Fig. 1(b).

At the fastest timescale, a two-dimensional finite-difference time-domain (FDTD) solver propagates the optical or electrically injected field through the nanostructured geometry, with the dielectric response of both the metal grating and the TMD excitonic resonances represented through auxiliary differential equation (ADE) polarization currents derived from a multi-pole Lorentz-Drude model;[18, 19] this captures the frequency-dependent absorption and near-field enhancement produced by localized surface plasmon resonances of the grating without requiring frequency-domain post-processing. For the PL simulations, because the nanorod array is periodic, Bloch (split-field) boundary conditions are imposed at the lateral domain edges so that a single unit cell can be simulated under arbitrary incidence angle, while perfectly matched layers absorb outgoing radiation at the top and bottom of the domain; illumination is introduced through a total-field/scattered-field formulation that cleanly separates the incident plane wave from the fields scattered by the grating and the TMD sheet. The electromagnetic solution yields two physically distinct quantities that couple the fast optical timescale to the slower material response: a spatially resolved optical generation rate, obtained from the dissipated power associated with the imaginary part of the TMD permittivity, and a Purcell factor, obtained from an auxiliary dipole-source FDTD calculation that compares the radiated power of a point emitter at the TMD plane in the presence of the grating to its free-space value. The Purcell factor renormalizes the radiative lifetime entering the exciton dynamics, providing the mechanism by which the plasmonic environment enhances (or, at unfavorable spacing, quenches) the emitted light.

At an intermediate timescale, the optical generation rate feeds a drift-diffusion solver that tracks free electron and hole densities and their transport under a self-consistently computed electrostatic potential, obtained by solving Poisson's equation with the local, spatially varying permittivity of the metal, TMD, and substrate regions. Because the exciton binding energy in monolayer TMDs is much larger than the thermal energy at room temperature, photogenerated free carriers are converted essentially instantaneously into bound excitons, so the drift-diffusion layer supplies a generation source directly to a set of excitonic rate equations rather than allowing a long-lived free-carrier population to persist. These rate equations track the areal densities of bright and dark excitons at the slowest timescale, including radiative and non-radiative decay, exciton-exciton annihilation, and thermally activated bright-dark interconversion enforced by detailed balance; the radiative decay term uses the Purcell-renormalized lifetime obtained from the electromagnetic layer, so the plasmonic enhancement of the local density of optical states is transmitted self-consistently into the exciton population dynamics and, ultimately, into the emitted spectrum.

The three timescales are reconciled through an operator-splitting outer loop rather than by resolving them on a common time grid, which would be computationally prohibitive given their disparate scales (sub-femtosecond optical cycles versus picosecond-to-nanosecond exciton dynamics). Within each outer step, many FDTD subcycles are advanced to accumulate a cycle-averaged field intensity and generation rate; these averaged quantities are then held fixed while the drift-diffusion and excitonic layers are advanced using an implicit update that accommodates the nonlinear exciton-exciton annihilation term. The resulting bright-exciton population is converted into an incoherent emission source amplitude that is reinjected as a dipole current into the electromagnetic layer for the next block of FDTD subcycles, closing the loop between emission and re-propagation through the plasmonic grating. This scheme allows the fast electromagnetic response of the grating, the picosecond-scale carrier transport, and the nanosecond-scale exciton recombination to be evolved concurrently at their own natural timescales while remaining fully coupled, yielding spatially and spectrally resolved predictions of grating-enhanced PL and EL from the 2D material layer.

The frequency-dependent permittivity of both the MoS_2 monolayer and the Au nanostructures is represented using a Lorentz–Drude model of the form

$$\varepsilon(\omega) = \varepsilon_\infty - \frac{\omega_{p,D}^2}{\omega^2 + i\omega\gamma_D} + \sum_k \frac{\Delta\varepsilon_k\, \omega_{p,k}^2}{\omega_{p,k}^2 - \omega^2 - i\omega\gamma_k}, \tag{1}$$

where ε_∞ is the high-frequency background permittivity, $\omega_{p,D}$ and γ_D are the Drude plasma and collision frequencies (used for Au only), and each Lorentz pole k is described by a resonance energy $\hbar\omega_{p,k}$, damping $\hbar\gamma_k$, and oscillator strength $\Delta\varepsilon_k$. For MoS_2, five Lorentz poles are used with no Drude term, since the monolayer is treated as a non-metallic dispersive medium. Table 1 summarizes the material, excitonic, and transport parameters used to model monolayer MoS_2 in the coupled FDTD–excitonic solver.

Table 1: Material and excitonic parameters used for monolayer MoS_2.

Parameter	**Symbol**	**Value**
Basic material properties		
Monolayer thickness	d	0.65 nm
Direct bandgap	E_g	1.85 eV
Intrinsic areal carrier density	n_i	10^3 cm^{-2}
Lorentz–Drude dispersion		
Background permittivity	ε_∞	3.23
Resonance energies	$\hbar\omega_{p,k}$	1.876, 2.024, 2.891, 4.110, 5.145 eV
Damping energies	$\hbar\gamma_k$	0.036, 0.119, 0.496, 0.715, 1.384 eV
Oscillator strengths	$\Delta\varepsilon_k$	0.195, 0.605, 6.415, 2.155, 1.611
Excitonic parameters		
Radiative lifetime	τ_r	1.0 ns
Non-radiative lifetime (as-exfoliated)	τ_{nr}	100 ps
Dark-exciton non-radiative lifetime	$\tau_{nr,D}$	100 ps
Exciton formation time	τ_{form}	1.0 ps
Bright–dark splitting	ΔE_{BD}	14 meV
Bright-to-dark scattering rate	k_{BD}	10^{10} s^{-1}
Exciton–exciton annihilation coefficient	γ_{EEA}	10^{-2} cm^2/s
Exciton diffusion coefficient	D_X	2.0 cm^2/s
Mott density	n_{Mott}	10^{13} cm^{-2}
Transport parameters		
Electron mobility	μ_n	50 cm^2/(V·s)
Hole mobility	μ_p	5 cm^2/(V·s)
Electron lifetime	τ_{n0}	0.5 ns
Hole lifetime	τ_{p0}	0.5 ns

3. NUMERICAL RESULTS

The simulation domain is discretized on a two-dimensional Yee grid with spatial steps $dx = 3.25$ nm and $dy = 0.65$ nm, the latter chosen to resolve the monolayer thickness. The domain consists of, from top to bottom, an air region of thickness 200 nm, the monolayer TMD, and a SiO_2 substrate of thickness 200 nm. Periodic boundary conditions are imposed on the left and right domain boundaries to represent an infinite nanostructure array, while a perfectly matched layer (PML) of 15 cells truncates the top and bottom boundaries to absorb outgoing radiation. The background dielectric constants are taken as $\varepsilon_{\text{air}} = 1.0$ and $\varepsilon_{SiO_2} = 2.1$. The outer-loop time integration was carried out for a total simulated duration of 800 ps for the MoS_2 simulations and 1200 ps for the WSe_2 simulations, discretized into 16k and 24k outer time steps, respectively (corresponding to an outer step size of 50 fs in both cases). The wavelength and peak excitation intensity are 532 nm and 1 kW/cm^2, respectively. The electric field of the incident light is polarized along the x-direction (P polarization), and the excitation propagates along the y-direction.

We first study the PL in the absence of the Au grating. Fig. 2(a) shows the normalized electric field magnitude, $|E|$, computed on the Yee mesh, spanning the substrate, the monolayer MoS_2, and the superstrate (air). This field profile serves as the electromagnetic backdrop into which the exciton dipole emission channels are embedded in the coupled FDTD/drift-diffusion/excitonic framework, and underlies the PL spectra and time-dependent intensities as follows. Figures 2(b) and 2(c) present, respectively, the steady-state PL spectrum as a function of luminescence wavelength and the time-resolved average PL intensity computed for monolayer MoS_2 and WSe_2 within our multiscale FDTD/drift-diffusion/excitonic framework. Fig. 2(b) shows that WSe_2 exhibits a narrow, intense peak centered near 740 nm, while MoS_2 produces a much weaker and considerably broader A-exciton feature centered near 660 nm, with a peak-to-peak intensity ratio of approximately 9:1. This large disparity in the normalized spectral peak, however, does not directly reflect the relative amount of light emitted by the two materials, since it does not account for the substantially different linewidths of the two transitions. Fig. 2(c) resolves this ambiguity by tracking the average PL intensity as a function of time following excitation, which is proportional to the wavelength-integrated (i.e., total) radiated power at each instant. Both curves rise from zero and saturate to a steady-state value as the exciton populations reach quasi-equilibrium between generation and radiative/non-radiative recombination channels. MoS_2 approaches its steady-state value more rapidly, reaching saturation within $\sim$500 picoseconds, consistent with a shorter effective exciton lifetime, whereas WSe_2 rises more slowly and saturates only after nearly a nanosecond, yet ultimately reaches a substantially higher steady-state intensity, reflecting its higher radiative efficiency. At steady state, the ratio of the saturated average intensities is approximately 5.3:1 (WSe_2:MoS_2), markedly smaller than the 9:1 ratio suggested by the peak spectral amplitude alone. This reduction is a direct consequence of the substantially broader MoS_2 emission linewidth seen in Fig. 2(b), which compensates part of the peak-intensity deficit once the spectral weight is integrated over wavelength (or, equivalently, once the full exciton population dynamics are integrated over time). The two materials differ not only in their steady-state emission efficiency but also in their underlying population dynamics, with MoS_2 exhibiting faster buildup/decay kinetics and WSe_2 exhibiting slower kinetics but higher radiative output.

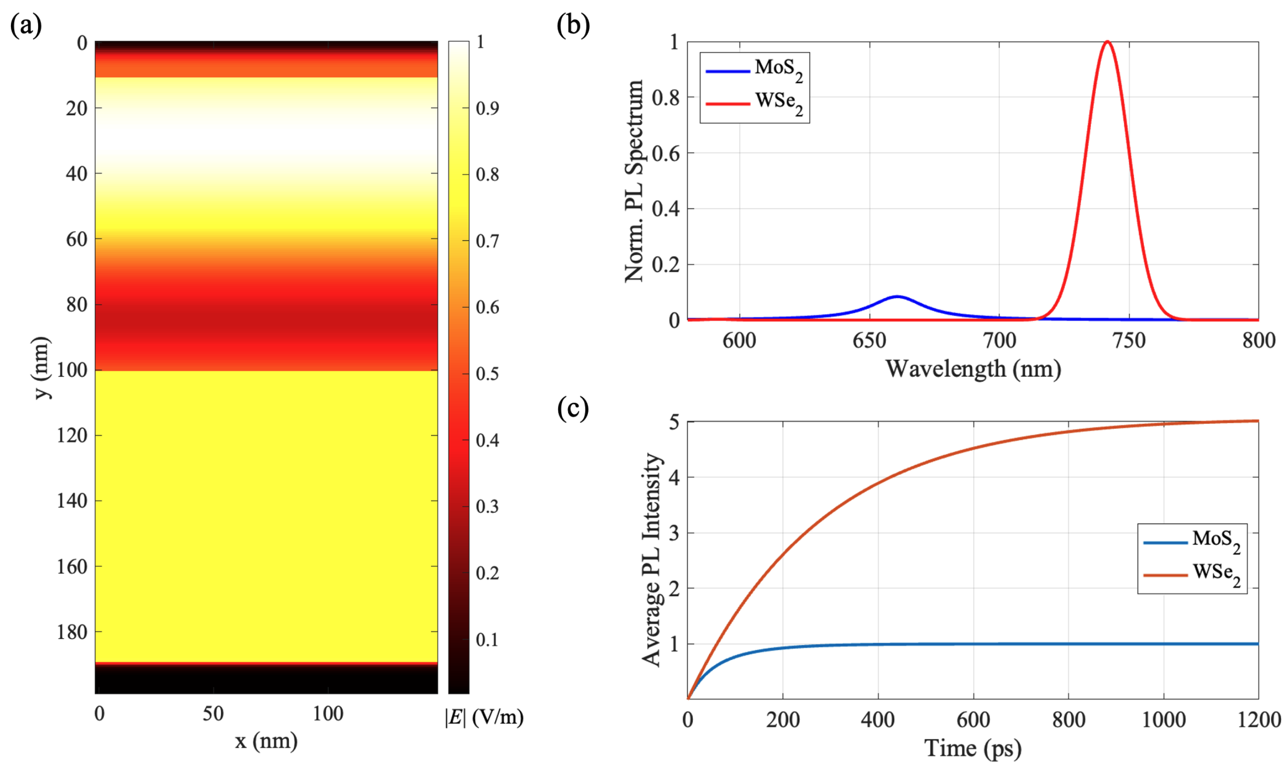

Figure 2: Baseline (bare monolayer) simulation results from the multiscale FDTD/drift-diffusion/excitonic framework. (a) Normalized electric field intensity distribution over the Yee mesh. The monolayer MoS_2 is at $y = 100$ nm. (b) PL spectrum as a function of emission wavelength and (c) average PL intensity as a function of time for monolayers of MoS_2 (blue) and WSe_2 (red)

These steady-state results reveal several physically meaningful trends beyond the overall PL intensity ratio reported above. Although 532 nm excitation lies far closer to the B-exciton resonance than the A-exciton resonance in both materials, nearly all of the photogenerated population is ultimately funneled into the A-exciton channel prior to recombination: the B-exciton radiative rate accounts for less than 1% of the total radiative rate in both MoS_2 ($R_{\mathrm{rad},B}/R_{\mathrm{rad,total}} \approx 0.8\%$) and WSe_2 ($\approx 0.2\%$), despite the B channel absorbing over 95% of the total generation rate (G_B/G_{ss}) in both materials. This confirms that the framework correctly captures a fast B-to-A relaxation cascade, with essentially all steady-state emission originating from the lowest-energy bright exciton regardless of which manifold is initially populated by the pump. The overall quantum yield is roughly three times larger in WSe_2 (0.142) than in MoS_2 (0.047), a smaller disparity than the ∼5.3-fold difference in total radiative rate $R_{\mathrm{rad,total}}$, consistent with the overall PL intensity ratio reported above. Finally, the free-carrier sheet densities $n_{\mathrm{sheet}}, p_{\mathrm{sheet}}$ remain five orders of magnitude smaller than the total exciton densities $N_B + N_D$ in both materials, providing direct numerical confirmation that photogenerated carriers are converted essentially instantaneously into bound excitons, consistent with the large exciton binding energy assumed in the model.

For the plasmonic enhancement study, we assume that each Au nanorod has a width of 60 nm and a height of 30 nm, arranged with a period of 150 nm along x-direction. For Au, the model uses a single Drude pole[18] with $\hbar\omega_{p,D}$ corresponding to $\omega_{p,D} = 1.3650 \times 10^{16}$ rad/s and $\gamma_D = 1.0500 \times 10^{14}$ rad/s, together with two interband Lorentz poles at resonance energies of 3.70 eV and 2.95 eV, damping of 0.87 eV and 1.09 eV, and oscillator strengths of 1.11 and 0.27, respectively. Figure 3 presents the plasmonic enhancement results for MoS_2 PL under a gold (Au) grating.

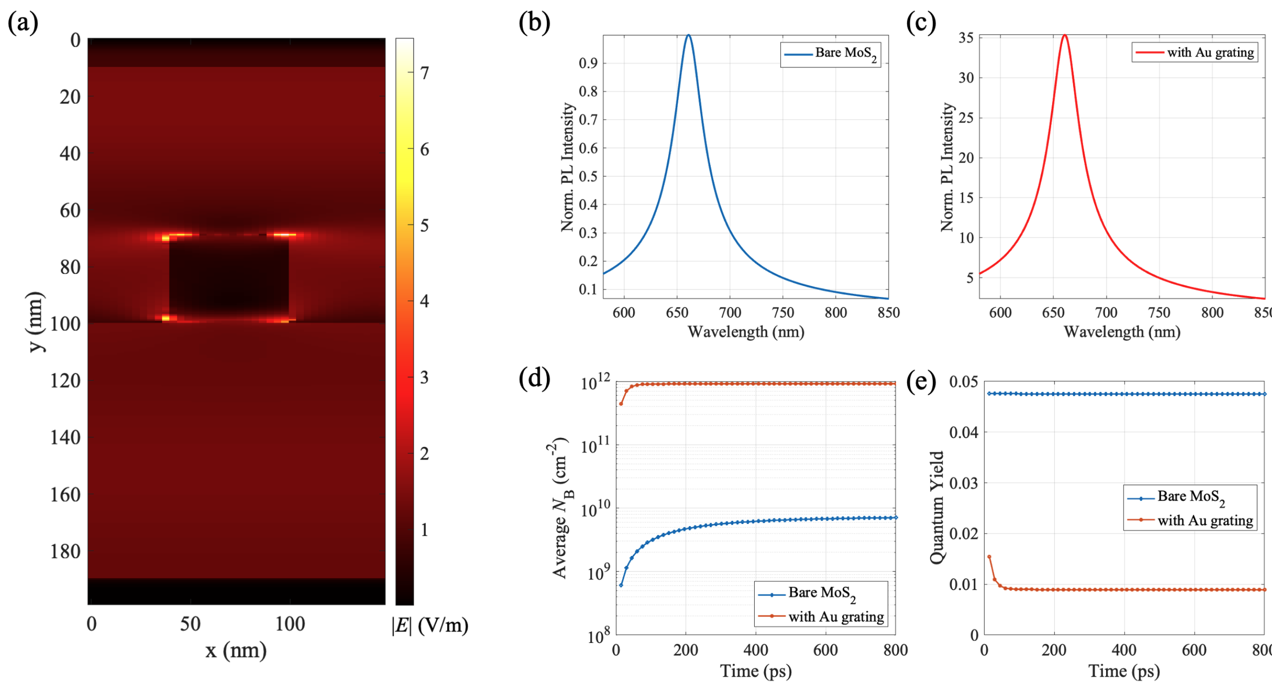

Figure 3: Plasmonic enhancement simulation results for MoS_2 coupled to an Au grating. (a) Electric field intensity distribution, $|E|$, over the Yee mesh, showing strong field enhancement localized at the corners of the Au nano-rod. PL spectra as a function of emission wavelength for (b) bare MoS_2 and (c) MoS_2 with the Au grating, both peaking near 660 nm but differing by roughly a factor of 35 in peak intensity. (d) Average bright-exciton population, N_B, and (e) internal quantum yield as functions of time for the bare and Au-grating cases. Despite a two-order-of-magnitude increase in the bright-exciton population with the Au grating, the overall PL enhancement is limited to ∼35× due to a concomitant decrease in quantum yield, reflecting the interplay between plasmonically enhanced absorption/generation and metal-induced non-radiative quenching.[4]

Panel (a) shows the electric field magnitude distribution over the Yee mesh in the vicinity of the grating; the field is strongly localized at the corners of the Au grating bars, where sharp geometric features produce lightning-rod-type field concentration, while the field inside and directly beneath the metal is largely screened. This near-field hot-spot behavior is the physical origin of the enhanced light–matter interaction discussed below.

Panels (b) and (c) compare the normalized PL spectra of bare MoS_2 and MoS_2 coupled to the Au grating, respectively; both spectra retain the same A-exciton peak position near 660 nm, indicating that the grating does not appreciably shift the emission energy, but the peak PL intensity increases from a normalized value of 1 in the bare case to approximately 35 with the grating, corresponding to roughly a 35-fold enhancement in emitted intensity. Panels (d) and (e) explain the physical origin of this enhancement by tracking the average bright-exciton population, N_B, and the internal quantum yield as functions of time. The Au grating increases the steady-state bright-exciton population by roughly two orders of magnitude relative to the bare case, consistent with strong near-field-enhanced absorption and carrier generation at the plasmonic hot spots identified in panel (a). However, the quantum yield with the grating is markedly lower than in the bare case, dropping from about 0.047 to about 0.009 once steady state is reached, reflecting the introduction of additional non-radiative decay channels (e.g., metal-induced quenching) that compete with the enhanced radiative decay. The net 35-fold PL enhancement therefore results from the multiplicative combination of these two competing effects: a $\sim 2 \times 10^2$-fold increase in the bright-exciton population is partially offset by a ~ 5-fold reduction in quantum yield, yielding a much more modest, though still substantial, overall PL enhancement. This highlights that plasmonic enhancement of 2D-material emitters is governed by a balance between excitation/absorption enhancement and non-radiative loss, rather than by either effect in isolation. Beyond the steady-state values, the transient buildup of N_B in Fig. 3(d) itself provides direct evidence of Purcell-accelerated radiative recombination: bare MoS_2 requires $\sim$500 ps to reach saturation, whereas the Au-grating case saturates roughly five times faster, in $\sim$100 ps, reflecting the shortened effective exciton lifetime imposed by the enhanced local density of optical states at the plasmonic hot spots. This trend is in direct qualitative agreement with time-resolved PL measurements by Gautam *et al.*, who reported a reduction in the room-temperature PL lifetime from 0.595 ns for pristine MoS_2 to 0.130 ns for Au-grating-decorated MoS_2,[8] and with Kim *et al.*, who similarly observed Purcell-enhanced photoluminescence and accelerated radiative decay in few-layer MoS_2 transferred onto plasmonically resonant Au nanostructure arrays.[6] The consistency between our simulated saturation-time acceleration and these experimentally measured lifetime reductions lends further support to the physical validity of the Purcell-renormalization mechanism implemented in our excitonic rate-equation layer.

It is worth contextualizing the magnitude of the enhancement obtained here relative to the highest values reported in the experimental literature. Gautam *et al.* achieved PL enhancement exceeding 390-fold using an optimized, ultra-thin Au grating (818 nm pitch, 2.6 nm thickness);[8] the extreme thinness of this grating is central to its performance, as it is sufficient to support a strong plasmonic near field while minimizing the metal volume available for Ohmic absorption and non-radiative quenching. The grating geometry used in the present simulations (60 nm width, 30 nm height, 150 nm period) is considerably narrower in pitch and substantially thicker than this optimized experimental design, and was chosen not to maximize PL enhancement but to provide a numerically well-resolved, physically representative test geometry for validating the self-consistent electromagnetic–transport–excitonic coupling scheme itself. Consequently, the more modest $\sim$35-fold enhancement obtained here should be interpreted as a demonstration of the framework's ability to capture the correct qualitative and mechanistic trends (near-field enhancement, Purcell acceleration, and non-radiative quenching acting in competition), rather than as an attempt to reproduce or exceed the largest enhancement factors reported experimentally; systematic optimization of the grating thickness, pitch, and material, informed by this same framework, is a natural direction for future work.

We further find that the plasmonic PL enhancement reported above is strongly polarization-dependent. The results presented in Fig. 3 correspond to the P polarization in which the electric field orientation is vertical to the metal nanorods of the grating, e.g., $\mathbf{E}_{\text{inc}} = \hat{x}E_0$ and nanorods are assumed to be infinitely long along the z-axis. In this configuration, the Au grating supports strong localized surface plasmon resonances at its edges, as seen in the near-field hot spots of Fig. 3(a), which drive the enhanced absorption and Purcell-accelerated emission discussed above. In contrast, under the S polarization (E_z out of plane, in-plane H_x, H_y), the grating geometry considered here does not support an analogous in-plane plasmonic resonance, and no significant PL enhancement was observed with the Au grating; moreover, an Ag grating of the same geometry produced a net PL quenching under this illumination, indicating that in this polarization the additional non-radiative decay channels introduced by the metal (Ohmic loss, near-field damping) dominate over any near-field or Purcell contribution to the radiative rate. This polarization dependence underscores that the sign and magnitude of plasmonic PL enhancement in grating geometries of this type are governed not only by the choice of metal and grating dimensions but also by the orientation of the exciting field relative to the grating periodicity, a distinction that is naturally and self-consistently captured within our FDTD-based electromagnetic layer.

Future work will extend the framework to explicitly include hot-electron/charge-transfer doping effects, apply it to the geometry optimization of grating thickness, pitch, and material composition toward the higher enhancement factors reported experimentally, and validate its electroluminescence predictions against injection-driven light-emitting device measurements.

4. CONCLUSION

We have developed a multiscale FDTD/drift-diffusion/excitonic-density simulation framework that self-consistently couples electromagnetic near-field enhancement, Purcell-renormalized radiative decay, and bright/dark exciton population dynamics to predict plasmonically enhanced photoluminescence from monolayer TMDs. By operator-splitting the fast optical-cycle timescale from the picosecond-to-nanosecond timescales of carrier transport and exciton recombination, the framework evolves all three physical layers concurrently while remaining fully bidirectionally coupled, with cycle-averaged generation rates and Purcell factors from the electromagnetic solver feeding the exciton rate equations, and the resulting bright-exciton population sourcing an incoherent dipole current that re-enters the electromagnetic domain. Applied to bare monolayer MoS_2 and WSe_2, the framework correctly captured qualitatively distinct emission behaviors between the two materials, showing that the naive 9:1 contrast in peak PL amplitude overstates the true, wavelength-integrated difference in emitted intensity, which is closer to 5.3:1 once the substantially broader MoS_2 linewidth and its faster population dynamics are properly accounted for. Applied to MoS_2 coupled to a periodic Au grating, the framework reproduced the essential physics of plasmonic PL enhancement, showing that a $\sim$35-fold increase in emitted PL arises from the multiplicative combination of a $\sim 2 \times 10^2$-fold increase in the bright-exciton population and a $\sim$ 5-fold reduction in internal quantum yield due to metal-induced non-radiative quenching, and that the accompanying $\sim$5-fold acceleration of the exciton population buildup time is in good qualitative agreement with Purcell-lifetime reductions measured experimentally in analogous Au-grating and Au-nanostructure-array geometries. The framework additionally reproduced the polarization dependence of plasmonic PL enhancement intrinsic to grating geometries, showing appreciable enhancement only under P polarization illumination, where the grating supports localized surface plasmon resonances, and negligible enhancement, or even quenching, under S polarization illumination, where non-radiative metal losses dominate in the absence of a supporting in-plane resonance. Our results demonstrate that the proposed framework captures, within a single self-consistent simulation, the competing near-field-enhancement, Purcell-acceleration, and non-radiative-quenching channels identified across the experimental literature as governing plasmonic PL enhancement in 2D materials, providing a predictive computational tool for the rational design of plasmonically enhanced 2D-material light emitters.

REFERENCES

[1] Mak, K. F., Lee, C., Hone, J., Shan, J., and Heinz, T. F., "Atomically thin MoS_2: A new direct-gap semiconductor," *Phys. Rev. Lett.* **105**, 136805 (2010).

[2] Splendiani, A., Sun, L., Zhang, Y., Li, T., Kim, J., Chim, C.-Y., Galli, G., and Wang, F., "Emerging photoluminescence in monolayer MoS_2," *Nano Lett.* **10**, 1271–1275 (2010).

[3] Lee, K. C. J., Chen, Y.-H., Lin, H.-Y., Cheng, C.-C., Chen, P.-Y., Wu, T.-Y., Shih, M.-H., Wei, K.-H., Li, L.-J., and Chang, C.-W., "Plasmonic gold nanorods coverage influence on enhancement of the photoluminescence of two-dimensional MoS_2 monolayer," *Scientific Reports* **5**, 16374 (2015).

[4] Mukherjee, B., Kaushik, N., Tripathi, R. P. N., Joseph, A. M., Mohapatra, P. K., Dhar, S., Singh, B. P., Kumar, G. V. P., Simsek, E., and Lodha, S., "Exciton emission intensity modulation of monolayer MoS_2 via Au plasmon coupling," *Scientific Reports* **7**(1), 41175 (2017).

[5] Yan, J., Ma, C., Liu, P., and Yang, G., "Plasmon-induced energy transfer and photoluminescence manipulation in MoS_2 with a different number of layers," *ACS Photonics* **4**(5), 1092–1100 (2017).

[6] Kim, H., Moon, S., Kim, J., Nam, S. H., Kim, D. H., Lee, J. S., Kim, K.-H., Kang, E. S. H., Ahn, K. J., Kim, T., Shin, C., and Suh, Y. D., "Purcell-enhanced photoluminescence of few-layer MoS_2 transferred on gold nanostructure arrays with plasmonic resonance at the conduction band edge," *Nanoscale* **13**(10), 5316–5323 (2021).

[7] Irfan, I., Golovynskyi, S., Yeshchenko, O. A., Bosi, M., Zhou, T., Xue, B., Li, B., Qu, J., and Seravalli, L., "Plasmonic enhancement of exciton and trion photoluminescence in 2D MoS2 decorated with Au nanorods: Impact of nonspherical shape," *Physica E: Low-dimensional Systems and Nanostructures* **140**, 115213 (2022).

[8] Gautam, C., Yadav, S., Kumar, A., Pal, M., Ghosh, A. K., and Giri, A., "Plasmonic grating on monolayer MoS_2 for strong photoluminescence enhancement and ultrasensitive surface-enhanced raman scattering (SERS) detection," *Nano Letters* **25**, 17152–17159 (2025).

[9] Jiang, Y., Wang, H., Wen, S., Chen, H., and Deng, S., "Resonance coupling in an individual gold nanorod–monolayer WS_2 heterostructure: Photoluminescence enhancement with spectral broadening," *ACS Nano* **14**, 13841–13851 (2020).

[10] You, Q., Li, Z., Li, Y., Qiu, L., Bi, X., Zhang, L., Zhang, D., Fang, Y., and Wang, P., "Resonance photoluminescence enhancement of monolayer MoS_2 via a plasmonic nanowire dimer optical antenna," *ACS Applied Materials & Interfaces* **14**, 23756–23764 (2022).

[11] Taflove, A. and Hagness, S. C., [*Computational Electrodynamics: The Finite-Difference Time-Domain Method*], Artech House, Norwood, MA, 3rd ed. (2005).

[12] Islam, R., Anjum, I. M., Menyuk, C. R., and Simsek, E., "Study of an MoS_2 phototransistor using a compact numerical method enabling detailed analysis of 2D material phototransistors," *Sci. Rep.* **14**, 15269 (2024).

[13] Islam, R., Anjum, I., Menyuk, C. R., and Simsek, E., "2D material-based plasmonic phototransistors under strong optical excitations," *J. Comput. Electron.* **24**, 104 (2025).

[14] Simsek, E., Anjum, I. M., Carruthers, T. F., Menyuk, C. R., Campbell, J. C., Tulchinsky, D. A., and Williams, K. J., "Fast evaluation of RF power spectrum of photodetectors with windowing functions," *IEEE Trans. Electron Devices* **70**, 3643–3648 (July 2023).

[15] Scharfetter, D. L. and Gummel, H. K., "Large-signal analysis of a silicon Read diode oscillator," *IEEE Trans. Electron Devices* **16**, 64–77 (1969).

[16] Palummo, M., Bernardi, M., and Grossman, J. C., "Exciton radiative lifetimes in two-dimensional transition metal dichalcogenides," *Nano Lett.* **15**, 2794–2800 (2015).

[17] Wang, H., Zhang, C., Chan, W., Manolatou, C., Tiwari, S., and Rana, F., "Radiative lifetimes of excitons and trions in monolayers of the metal dichalcogenide MoS_2," *Phys. Rev. B* **93**, 045407 (2016).

[18] Rakić, A. D., Djurišić, A. B., Elazar, J. M., and Majewski, M. L., "Optical properties of metallic films for vertical-cavity optoelectronic devices," *Applied Optics* **37**(22), 5271–5283 (1998).

[19] Mukherjee, B., Tseng, F., Gunlycke, D., Amara, K. K., Eda, G., and Simsek, E., "Complex electrical permittivity of the monolayer molybdenum disulfide (MoS_2) in near UV and visible," *Opt. Mater. Express* **5**(2), 447–455 (2015).